Machine learning for improvement of upper tropospheric relative humidity in ERA5 weather model data

Ziming Wang[1,2], Luca Bugliaro[1], Klaus Gierens[1], Michaela I. Hegglin[3,4], Susanne Rohs[5], Andreas Petzold[5], Stefan Kaufmann[1], Christiane Voigt[1,2]

[1]Institute of Atmospheric Physics, Deutsches Zentrum für Luft- und Raumfahrt (DLR), Oberpfaffenhofen, 82234, Germany
[2]Institute of Atmospheric Physics, Johannes Gutenberg University Mainz, Mainz, 55128, Germany
[3]Institute of Energy and Climate Research, IEK-7: Stratosphere, Forschungszentrum Jülich, Jülich, 52428, Germany
[4]Department of Meteorology, University of Reading, Reading, RG6 6ET, United Kingdom
[5]Institute of Energy and Climate Research, IEK-8: Troposphere, Forschungszentrum Jülich, Jülich, 52428, Germany

Correspondence to: Ziming Wang (Ziming.Wang@dlr.de)

Abstract. Knowledge of humidity in the upper troposphere and lower stratosphere (UTLS) is of special interest due to its importance for cirrus cloud formation and its climate impact. However, the UTLS water vapor distribution in current weather models is subject to large uncertainties. Here, we develop a dynamic-based humidity correction method using artificial neural network (ANN) to improve the relative humidity over ice (RHi) in ECMWF numerical weather predictions. The model is trained with time-dependent thermodynamic and dynamical variables from ECMWF ERA5 and humidity measurements from the In-service Aircraft for a Global Observing System (IAGOS). Previous and current atmospheric variables within ±2 ERA5 pressure layers around the IAGOS flight altitude are used for ANN training. RHi, temperature and geopotential exhibit the highest impact on ANN results, while other dynamical variables are of low to moderate or high importance. The ANN shows excellent performance and the predicted RHi in the UT has a mean absolute error MAE of 5.7% and a coefficient of determination R^2 of 0.95, which is significantly improved compared to ERA5 RHi (MAE of 15.8%; R^2 of 0.66). The ANN model also improves the prediction skill for all sky UT/LS and cloudy UTLS and removes the peak at RHi = 100%. The contrail predictions are in better agreement with MSG observations of ice optical thickness than the results without humidity correction for a contrail cirrus scene over the Atlantic. The ANN method can be applied to other weather models to improve humidity predictions and to support aviation and climate research applications.

1 Introduction

The atmospheric region of the upper troposphere and lower stratosphere (UTLS) in the tropics (Dessler and Sherwood, 2009) and the extratropics (Gettelman et al., 2011) plays a crucial role in the climate system. Within the UTLS, atmospheric humidity significantly influences the radiation budget at the top-of-atmosphere (TOA) (Riese et al., 2012). In fact, water vapor is the dominant atmospheric long-wave absorber in the context of the global greenhouse effect (Schmidt et al. 2010). Further, observed increases in stratospheric water vapor (Hegglin et al., 2014) contribute to both stratospheric cooling and tropospheric warming (Forster and Shine, 2002), and act as positive feedback to surface temperature (Tao et al., 2023). Relative humidity

(RH) over ice (RHi) > 100% or ice supersaturation is of major importance for the formation and persistence of natural cirrus and aircraft-induced contrail cirrus (Kärcher, 2018). Cirrus in this region can survive for hours if ambient conditions are ice supersaturated (Zhao et al., 2023) and they can have a positive cloud radiative effect on climate (Gazparini et al., 2020). Hence, accurate observations and representations of UTLS water vapor (Hegglin et al., 2014) are essential for climate and weather research.

During the past decades, many humidity measurements from aircraft in situ (Krämer et al., 2009; Diao et al., 2015; Kaufmann et al., 2018), lidar (Groß et al., 2014; Krüger et al., 2022), balloon-borne (Heymsfield et al., 1998; Dickson et al., 2010; Rollins et al., 2014) and polar orbiting satellite instruments (Lamquin et al., 2012; Hegglin et al., 2013) show that high RHi may often occur in the UT. However, these observations are limited in space and time, and the uncertainties are relatively high (Gierens et al., 2020). Important in situ humidity data can also be provided by in-service passenger aircraft (Petzold et al., 2020; Reutter et al., 2020), but three-dimensional fields of RHi and dynamics for large geographic regions are currently only available from numerical weather prediction (NWP) models, for instance the Integrated Forecasting System (IFS) at the European Centre for Medium-Range Weather Forecasts (ECMWF, 2016) and ICOsahedral Non-hydrostatic (ICON, Zängl et al., 2015; Seifert and Siewert, 2024) at the German Weather Service. A wet bias in the RHi of the extratropical LS has been identified in the operational ECMWF IFS forecast and analysis data, as observed in comparison with in situ measurements from research aircraft (Kaufmann et al., 2018) and from Civil Aircraft for the Regular Investigation of the atmosphere Based on an Instrument Container (CARIBIC) passenger aircraft flights (Dyroff et al., 2015). In contrast, a dry bias of RHi is observed in the cloudy UT when compared with aircraft measurements in the In-Service Aircraft for Global Observing System (IAGOS) (Teoh et al., 2022). The utilization of the saturation adjustment process (Tompkins et al., 2007), wherein supersaturation relaxes to saturation upon cloud formation, results in a systematic underestimation of both the frequency and magnitude of ice supersaturation at cruise altitudes within NWPs and global climate models (Sperber and Gierens, 2023).

There is ongoing debate on the physical explanations of the NWP humidity bias in the UTLS, which is a crucial factor to consider for the improvement of atmospheric humidity prediction. According to Kunz et al. (2014), the influences of dynamical transport processes are challenging for the simulations of ULTS humidity distribution. Backward trajectory analyses reveal a positive relationship between the moist bias at the aircraft flight level and air masses originating from high northern latitudes in the LS (Dyroff et al., 2015). The relationships between uncertainty in atmospheric mixing and the simulated composition of water vapor in the LS, as well as the radiative consequences in the UTLS, are highlighted by Krüger et al. (2022) and Riese et al. (2012), respectively. Small-scale stratospheric intrusions, which are frequently observed in the UTLS but are unsolved by the NWP model, are another possible source of moisture bias (Dyroff et al., 2015). Numerical diffusion, which can easily smoothen the gradients of humidity across the hydropause, is also a possible reason for the moist bias in the LS (Stenke et al., 2008). Interestingly, Woiwode et al. (2020) show that there is little dependency of the moist bias on temporal or vertical model resolution in the ECMWF IFS analysis and forecast data.

The assimilation of observations into NWP models is the state-of-the-art way to improve weather forecast (Lawrence et al., 2019; van der Linden et al., 2020). While as the primary data source for the assimilation system, calibrating RH instruments

at temperatures below 0°C is challenging, with the difficulty increasing as temperatures drop further. A great deal of effort has also been focused on post-processing of NWP data to improve the accuracy of atmospheric humidity and ice supersaturation prediction, as well as contrail cirrus, utilizing long-term aircraft measurements from IAGOS (Teoh et al., 2020; Wolf et al., 2023). Teoh et al. (2022) employ in situ measurements from IAGOS to formulate a correction method for ERA5 RHi fields.

70   With this method, the probability density function (PDF) of ERA5-corrected RHi inside ice supersaturation closely aligns with IAGOS measurements. Another humidity bias correction, also aiming to achieve consistency between IAGOS and ERA5 through a multivariate quantile approach, results in a notable reduction of the RHi bias (Wolf et al., 2023).

Gierens and Brinkop (2012) investigate the distributions of the dynamical quantities - divergence, relative vorticity, and vertical velocity from ECMWF IFS within and outside ice supersaturated regions and notice distinct patterns. Gierens et al.

75   (2020) postulate that a more accurate prediction of ice supersaturation in NWP models may be achievable by further incorporating dynamical atmospheric fields with ERA5 RHi in a general regression method. Wilhelm et al. (2022) also suggest a possibility to base an improved forecast of persistent contrails not only on the traditional quantities of temperature and RHi, but also on these dynamical proxies as well. In a recent study, Hofer et al. (2024) show that dynamical proxies taken only at the time and location of the forecast are insufficient for an improved prediction of ice supersaturation. However, they note the

80   potential for improving RHi predictions by incorporating additional forecast data from earlier time points and upstream areas. When improving the quality of meteorological data, machine learning techniques have been widely used nowadays. Kadow et al. (2020) have demonstrated the skill of artificial intelligence in reconstructing surface temperatures when combined with climate model data. A machine learning-based approach trained directly from historical NWP reanalysis data is introduced by Lam et al. (2023) to predict hundreds of weather variables at a remarkable speed. It outperforms the most accurate operational

85   systems on 90% of the verification tests, even without special consideration of vertical transport. Teoh et al. (2020) also suggest in their outlook on RHi correction that further effort can be made to explore machine learning techniques to improve the accuracy of the ERA5 humidity fields.

This paper aims at improving predictions of atmospheric humidity, in particular RHi and ice supersaturation, in the UTLS region starting from ERA5 fields using machine learning. The previous humidity corrections of Teoh et al. (2022) and Wolf

90   et al. (2023) for ERA5 model data were based on regression fitting methods using IAGOS observations but neglected the temporal evolution of dynamical quantities in the horizontal and vertical directions that led to the humidity bias. Targeting that gap, we develop an artificial neural network (ANN) model to correct relative humidity (and specific humidity in the supplement) from ERA5, leveraging thermodynamic conditions and dynamical quantities from ERA5, along with measured water vapor data from IAGOS above the Atlantic Ocean, Europe and Africa in 2020. The investigation is guided by three

95   specific questions:

1.   To what extent do atmospheric states impact the subsequent evolution of humidity fields?
2.   Is it feasible to develop a dynamic-based machine learning method to correct the humidity bias in the UTLS?
3.   How do the outcomes of the new method influence the ability to forecast ice supersaturation?

Finally, we apply the improved humidity fields for computing the optical properties of contrail cirrus in a particular situation using the Contrail Cirrus Prediction model (CoCiP) and compare the simulation results to satellite observations.

This paper is outlined as follows: Sect. 2 provides an overview of the IAGOS humidity measurements (Sect. 2.1), ERA5 and IFS data as input to the ANN model and for the application (Sect. 2.2), the collocation procedure of the measurement data with ERA5 (Sect. 2.3), and the initial comparison (Sect. 2.4), the contrail cirrus prediction model CoCiP (Sect. 2.5), and satellite remote sensing techniques for retrieving the microphysical properties of cirrus clouds (Sect. 2.6). In Sect. 3, the concept of the temporal dependence of RHi on the evolution of meteorological parameters, the development of the RHi improvement model, and the importance of the selected synoptic variables on RHi prediction are explained in detail. The evaluation of the RHi improvement model using different metrics is presented in Sect. 4. The corresponding information for specific humidity is provided in the supplement. Thereafter, Sect. 5 assesses the impact of the ANN humidity correction on the simulations of contrail cirrus in a case study. The conclusions are summarized in Sect. 6.

2 Data and application approaches

2.1 In-service Aircraft for a Global Observing System (IAGOS)

The In-service Aircraft for a Global Observing System (IAGOS; Petzold et al., 2015) is a European Research Infrastructure that implements instruments on long-range aircraft of internationally operating airlines for providing long-term in situ measurements of trace gases and meteorological conditions. These measurements are very valuable for the purpose of this study as most flight tracks are situated at heights between 9 and 13 km in the UTLS region. All aircraft within IAGOS have been equipped with a platinum sensor for temperature measurements with an accuracy of ±0.5 K, and a collocated capacitive sensor for monitoring RHi with an uncertainty of 5% to 10% (Petzold et al., 2020). The temperature detected at the sensor is transferred to the air temperature T_{IAGOS} by accounting for the (incomplete) adiabatic heating and the inlet heating. RHi is then derived using the measured water vapor mixing ratio, pressure, and T_{IAGOS} based on the saturation water vapor pressure equation from Sonntag (1994). The uncertainty of RHi increases with decreasing temperature due to a slower response time. In the dry conditions (RHi<10%) of the LS, the sensor has only limited accuracy (Rolf et al., 2023), so these data have been excluded for further evaluation. The temporal resolution of IAGOS measurements amounts to 4 s.
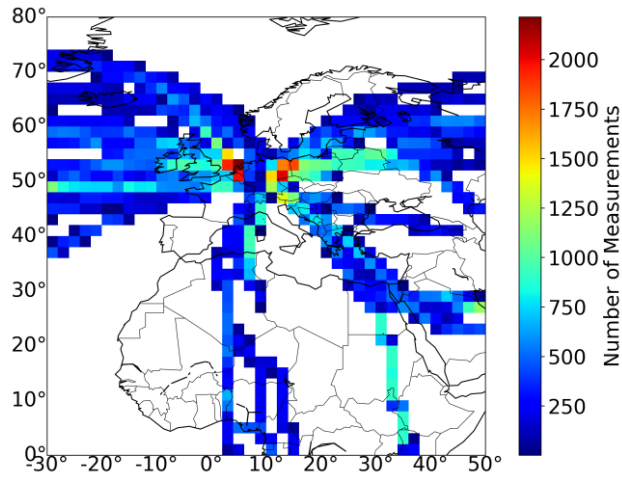
Figure 1: Number of IAGOS measurements per 2° × 2° latitude-longitude grid box between 200 hPa and 400 hPa over the Atlantic Ocean, Europe and Africa for the year 2020. The measurements are filtered based on data quality, details see the text.

The global distribution of IAGOS data is not uniform in every region since it is dependent on preferred flight routes and weather conditions. Western Europe and the eastern North Atlantic Region (NAR) show a high density in IAGOS data therefore we focus on this domain (Fig. 1, between 30°W and 50°E). We did not include the western regions of NAR, from where humid air is often advected, but instead focused on moisture originating and transported from lower atmospheric levels up to cruise altitude. In addition, we aim to cover the latitude range between 80°N and the equator because ice supersaturation occurs very frequently in the UT of the tropics. The geographic position of the aircraft, the time, data quality flags, ambient pressure, temperature T_{IAGOS} (Berkes et al., 2017), and RHi_{IAGOS} from IAGOS in the year 2020 are collected to produce the output humidity data set of the ANNs. We use only the IAGOS measurements that fulfill the following criteria: IAGOS quality flag is not "limited" or "invalid", and measurements are located between 0 and 80°N, and 30°W and 50°E, and between 400 and 200 hPa. The distribution of RHi_{IAGOS} shows high-density values that gradually decrease starting from 110% and drop significantly as they approach 150% (see Fig. S2 in the supplement), a trend consistent with findings in Wolf et al. (2023, Fig. 3) and Teoh et al. (2024, Fig. S4).

2.2 ECMWF reanalysis and forecast

Meteorological data for the year 2020 in the same region in Sect. 2.1 is sourced from the ERA5 reanalysis data, obtained from the ECMWF Copernicus Climate Data Store (Hersbach et al., 2020). The assimilation system takes new observations and combines them with IFS forecast data from 12 hours before the given time to make the best estimate of the current state of the atmosphere. ERA5 data is on an equidistant latitude-longitude grid of 0.25° resolution with an hourly output on 37 pressure levels. Hourly atmospheric parameters on pressure levels between 200 and 250 hPa with a 25-hPa spacing and between 250 and 400 hPa with a 50-hPa spacing are used for model training. The IFS forecast data (137 model levels) are used for predicting

145 contrail cirrus (see Sect. 5). Using pressure level data for ANN training reduces the size of the training dataset and saves model training time.

We use the following thermodynamic parameters from ERA5: temperature T_{ERA5}, and RHi_{ERA5} (in the main text) or specific humidity q_{ERA5} (in the supplement) as the inputs for the ANN model. The saturation water vapor pressure equation from Alduchov and Eskridge (1996) is used here to calculate RHi_{ERA5} from q_{ERA5}. In addition, specific cloud ice water content $ciwc$

150 from ERA5 is utilized to differentiate between the cirrus- and cirrus-free regions. $ciwc$ represents the mass of cloud ice particles per kilogram of moist air, averaged over a grid box. It is estimated using the prognostic equations of the cloud scheme (Tiedtke, 1993; Forbes and Tompkins, 2011; Forbes and Ahlgrimm, 2014), which account for cloud ice growth through deposition. As shown in Table 1, this study also considers dynamical parameters, including geopotential (z) for adiabatic shifts, vertical velocity (w) in Pa/s representing vertical air mass motion, divergence (d) indicating air spread or convergence, horizontal wind

155 speed (u and v) in m/s, and relative and potential vorticity (vo and pv) characterizing air rotation and stratosphere-troposphere exchanges. The use of pv specifically helps identify the dynamical tropopause and distinguish between UT and LS.

2.3 Data collocation

Table 1: Overview of the variables used in this study. Spatial resolution of ERA5: 0.25°. Vertical resolution of ERA5 on pressure levels: 25-50 hPa. The original temporal resolution of ERA5 and IAGOS: 1 h and 4 s. Study regions: Atlantic, Europe and Africa.

source	variable (* RHi ANN)	description	unit
ERA5 (7 conditions) • the current time and level • two time lags (-2h and -6h) • four ERA5 pressure levels surrounding the IAGOS cruise level (-2, -1, +1, +2)	* T_{ERA5}	air temperature	K
	$ciwc$	specific cloud ice water content	Kg/kg
	* RHi_{ERA5}	relative humidity w.r.t. ice	%
	q_{ERA5}	specific humidity	g/Kg
	* z	geopotential	m^2/s^2
	* w	vertical velocity	Pa/s
	* d	divergency of wind	s^{-1}
	* u	eastward component of wind	m/s
	* v	northward component of wind	m/s
	* vo	relative vorticity	s^{-1}
	pv	potential vorticity	s^{-1}
	time	hour	1
	level	pressure	hPa
IAGOS at the current time	* RHi_{IAGOS}	relative humidity w.r.t. ice	1
	T_{IAGOS}	air temperature	K
	pressure	air pressure	Pa

160 The ERA5 grid boxes that are closest to the IAGOS observations in both time and space are selected to align with the IAGOS measured humidity and temperature data sets between 400 hPa and 200 hPa. In contrast to other studies (Wolf et al., 2023; Hofer et al., 2024), this study also uses the temporal evolution of meteorological conditions before the IAGOS observation time. Specifically, RHi in the UTLS is influenced by horizontal and vertical air motions like air mass uplift (Diao et al., 2015) in convection or frontal systems, or stratospheric intrusions. To account for these, thermodynamic and dynamical data up to 6

165 h prior to the IAGOS data acquisition time, with 1h intervals, and within two pressure levels above and below the IAGOS acquisition location, are linked with RHi_{IAGOS} at the IAGOS acquisition time and location. These ERA5 variables are vertically interpolated to match the IAGOS location based on pressure levels. While the ERA5 data retains its original temporal and spatial resolution, the water vapor data measured by IAGOS, which includes several data points within a single ERA5 grid box, is averaged. This averaging reduces the autocorrelation in the measured data due to the response time of the sensor,

170 accounts for internal ERA5 grid box variability, and maintains a proportion of ice supersaturation after averaging. This collocation of model meteorological variables and measured humidity values from the year 2020 comprises 3.99 million individual data points. To ensure that the training set consists of data from time periods that do not overlap with those used for either validation and testing, we now use 4 days of data to build the ANN model, followed by a 1-day gap, and then 1 day of data for validation or testing. This method accounts for considerable variability and sharp gradients in the humidity fields, and

175 thus can help to estimate realistic atmospheric humidity distributions for comparisons and model application.

2.4 Initial ERA5 RHi evaluation using IAGOS

We first compare and quantify the difference between ERA5 and in situ measurements provided by IAGOS with respect to temperature, and specific and relative humidity. RHi in cirrus clouds in NWP can have a low bias due to the application of saturation adjustment in cloud parameterizations (ECMWF, 2016), hence we differentiate between model clear (cloudy)

180 conditions using *ciwc* equal to zero for all the current and ±2 pressure layers from ERA5. We further distinguish between UT (LS) dependent on the threshold *pv* smaller than 2 PVU. This means, we consider the dynamical tropopause as done for instance in Reutter et al. (2020). In the following, we focus on RHi (for comparison of other parameters, see also Sect. S1 and S4 in the supplement).
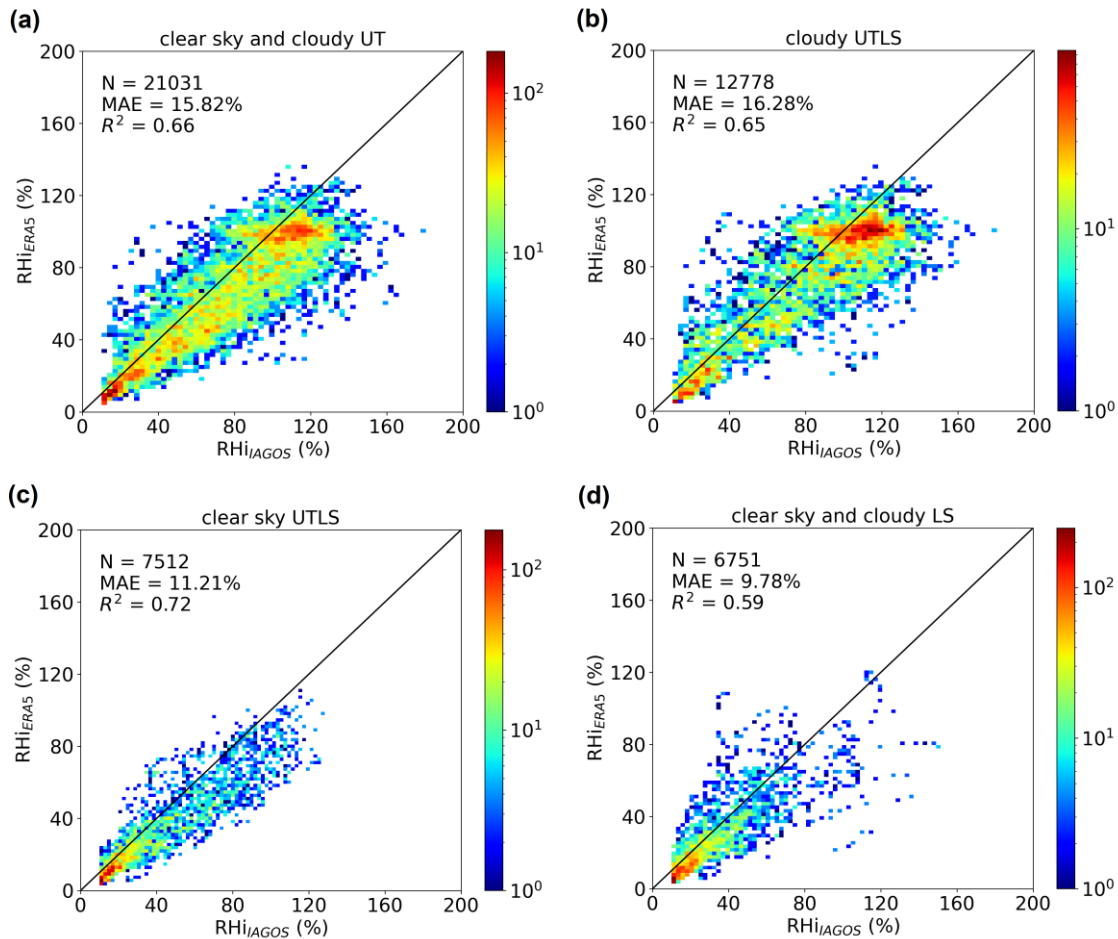
 Figure 2: Comparisons of RHi_{ERA5} against RHi_{IAGOS} in (a) clear sky and cloudy UT, (b) cloudy UTLS, (c) clear sky UTLS, and (d) clear sky and cloudy LS in the test data set between 200 hPa and 400 hPa over the Atlantic, Europe and Africa for the year 2020.

Figure 2 shows the comparison of RHi_{ERA5} and RHi_{IAGOS} separated either between upper troposphere or lower stratospheric conditions or between cloudy or clear sky conditions, respectively. Here we use the test dataset from the ERA5-IAGOS collection created in Sect. 2.3, which is the same dataset used for verifying the ANN model in Sect. 4.1. In the all sky UT (Fig. 2a) and in the cloudy UTLS (Fig. 2b), ERA5 RHi data show a considerably dry bias compared to IAGOS data, with mean absolute errors (MAEs) of 15.82% and of 16.28%, respectively. RHi and the magnitude of ice supersaturation in ERA5 are underestimated. In addition, a partially artificial occurrence accumulation peak exists in the ERA5 data set at RHi_{ERA5} = 100%. In RHi_{IAGOS}, a small peak is observed between 100% and 110% under cloudy conditions (Sanogo et al., 2024). However, much of the accumulation peak in the ERA5 data is attributed to the cloud saturation adjustment in NWP models. Nevertheless, RHi_{ERA5} > 100% is also observed, either in partly cloudy model boxes or in clear sky boxes, where only a fraction of the box is cloudy (with RHi_{ERA5}=100%) and the clear sky part is supersaturated, due to the time required for the

ice nucleation process. Consequently, RHi_{ERA5} values greater than 100% can occur in cloudy conditions as well. In the clear sky UTLS (Fig. 2c) and in the all sky LS (Fig. 2d) regions, MAEs are 11.21% and 9.78%, respectively. In the all sky LS (Fig. 2d), few RHi data > 100% have been measured by IAGOS, with most observations concentrated at low RHi values. In general, the extent and the degree of ice supersaturation underestimated by ERA5 are in line with the findings by Dyroff et al. (2015) for ECMWF analysis and forecast data. The comparison of ERA5 and IAGOS RHi serves as the motivation for our study, aiming to improve the humidity prediction by NWPs.

2.5 Contrail cirrus prediction model CoCiP

The Contrail Cirrus Prediction Model (CoCiP) is used to predict the contrail cirrus cover and examine the contrail radiative forcing induced by individual flights (Schumann, 2012; Schumann et al., 2017, 2021b; Voigt et al., 2017, 2022; Teoh et al., 2024). The contrail model uses traffic data from the North Atlantic Tracks for the Shanwick Oceanic Control Area. When the ambient temperatures fall below the Schmidt-Appleman criterion threshold (Schumann, 1996) at two successive flight waypoints, a contrail segment forms. Contrail initial water content, width, and depth are determined by aircraft properties and emissions (non-volatile particulate matter). Plume dispersion is a function of turbulence, wind shear, and induced heating. RHi inside contrail plumes is set at saturation, and ice water content of contrails grows or decreases in response to the ambient humidity. A Runge-Kutta integration simulates the contrail evolution until its end of life by ambient drying or particle losses from aggregation and sedimentation. The contrail life ends when the maximum contrail lifetime of 24 hours is reached, the ice number concentration is less than the background ice nuclei ($< 10^3$ m^{-3}), or the ice optical thickness (IOT) is less than 10^{-6}. CoCiP simulations account for humidity exchange between contrails and the background air, and the overlap of contrails above or below clouds present in the meteorological data from the NWP forecast (Schumann et al., 2021a). The CoCiP limitation in comparison to general circulation models is its absence of atmospheric interaction and feedback (Chen et al., 2012; Burkhardt et al., 2018; Bickel et al., 2020). In Sect. 5 of this study, we present an exemplary application of the model for RHi correction derived in this paper to contrail simulations and show its effect on contrail properties. This is done by performing two CoCiP runs: for the reference run, we use NWP data from ECMWF IFS for the contrail case on 14 April 2021 over the NAR within the ECLIF3 campaign (Märkl et al., 2024), for the second run we correct the NWP humidity data with the ANN proposed in this work in the same situation.

2.6 Satellite remote sensing

CoCiP simulations are compared to spaceborne data from the SEVIRI radiometer (3 km sampling distance at nadir) aboard the geostationary Meteosat Second Generation (MSG) satellite in Sect. 5. To derive ice cloud properties, CiPS (Cirrus Properties from SEVIRI, Strandgren et al. 2017) is used. It consists of a set of ANNs trained on SEVIRI thermal observations, CALIPSO (Cloud Aerosol Lidar and Infrared Pathfinder Satellite Observations) cloud products, ECMWF ERA-Interim surface temperature data and auxiliary data, to retrieve IOT for identified cirrus clouds. Specifically developed for thin cirrus clouds, CiPS has been validated against CALIPSO, achieving detection rates of 20%, 70%, and 85% for ice clouds with IOT

230 values of 0.01, 0.1, and 0.2, respectively. For IOT between 0.35 and 1.8, CiPS demonstrates a MAE smaller than 50%, and MAE increases for IOT values between 0.07 and 0.35.

3 ANN model development

3.1 The temporal dependence of measured humidity on individual meteorological parameters

Which meteorological parameters and at which time and pressure level should be chosen for training the RHi improvement
235 model? To answer this question, the dependence of measured RHi on meteorological variables at preceding times and surrounding pressure levels is considered by reviewing the sources of RHi bias in the UTLS within ECMWF data. As outlined in Dyroff et al. (2015), this bias is linked to air masses residing near the aircraft's flight level of approximately 230 hPa in high northern latitudes, likely influenced by airmass vertical intrusions and horizontal transport. This points out the connection between RHi and the temporal evolution of meteorological parameters.

240 Based on the physical definition of RHi, a negative correlation between RHi_{IAGOS} and T_{ERA5} is expected because RHi is the ratio of the partial vapor pressure of water vapor to the saturation vapor pressure with respect to ice, the latter of which increases with temperature. For dynamical variables, the positive relationship between increased geopotential z values and RHi_{IAGOS} is in accordance with the findings of Wilhelm et al. (2022). In addition, parameters such as vertical wind w, divergence d, horizontal wind speed components u and v, relative vorticity vo, and potential vorticity pv help represent the dynamical
245 conditions at a given time and place that influence relative humidity in the model. For instance, an upward motion (negative values of w in ERA5) results in cooling and a decrease in RHi, and promotes ice supersaturation. A relatively strong horizontal airmass movement with large divergence is typical for ice supersaturation. Large negative values of vorticity in anticyclonic systems are again also typical for supersaturation (Gierens et al., 2020). These connections suggest the potential to improve the RHi prediction by considering not only traditional thermodynamic variables like temperature but also dynamical proxies
250 and their temporal evolution. Further computations of the Pearson correlation coefficient between RHi_{IAGOS} and temporal meteorological variables from ERA5, and the impact of including data distributions from hours before the current time on improving the network prediction, are explained in Sect. S2.

To balance information richness and modeling efficiency, only the current IAGOS humidity fields, and ERA5 data at the current time of the IAGOS measurement, a 2-h and 6-h time lag prior to IAGOS data acquisition, as well as ±1, ±2 pressure
255 layers from ERA5 are selected as input variables to account for the typical lifespans of water vapor transport mechanisms, including deep convection, warm conveyor belt uplift regimes, and slow ascending flows (Wang et al., 2024). Notably, pv is not provided in ECMWF model level data and subsequently excluded from the input data set during further training of the ANN model. Summarising, the ANN model is trained with the variables shown in Table1. The relevance of each input atmospheric variable to the RHi prediction model developed in Sect. 3.2 is discussed in Sect. 3.3.

3.2 Development and training of the ANN model for humidity improvement

An ANN is composed of a large number of units that exchange information with each other, in a similar structure and function as neural networks in human brains. A basic ANN model contains three types of layers: an input layer, one or more hidden layer(s), and an output layer. Each layer is made up of neurons. Neurons receive the weighted sum of the results of the previous layer's neurons, use it as the argument of an activation function, and forward the results to the following layer. The feed-forward ANN used in this study employs a learning technique called back-propagation, where the outputs are compared to the target values to calculate the differences in the form of loss function. The error is then fed back to modify the weights and bias of each neuron based on the optimization method (see e.g. Ma et al., 2020).

Here, the ANN model for RHi is trained using a large set of atmospheric variables obtained from ERA5 reanalysis and RHi measured from IAGOS as explained in the previous section. The ANN learns to reproduce the nonlinear statistical relationships between the selected series of meteorological variables and humidity fields iteratively adjusting its parameters until it can robustly and accurately predict RHi in the UTLS. This procedure does not only consider RHi>100% to investigate ice supersaturation but also the full range of RHi to provide sufficient data for model building.

Based on the temporal dependence of measured humidity on individual meteorological parameters discussed in Sect. 3.1, the input variables for the ANN encompass RHi_{ERA5}, T_{ERA5}, and z, w, d, u, v, and vo. They are extracted from the ERA5 fields (Sect. 2.2) at the time of the IAGOS observation, as well as 2 h and 6 h prior, at the geographical and vertical location of the IAGOS measurement, along with ±1, ±2 ERA5 pressure levels. The output (target) variable of the ANN is RHi_{IAGOS}. The ANN model consists of 56 inputs, derived from 8 meteorological variables across 7 conditions: the current time and level, two time lags (-2 h and -6 h) for the current level and four ERA5 pressure levels surrounding the IAGOS cruise altitude (-2, -1, +1, +2 levels) for the current time. They are summarised in Table 1. We apply min-max normalization to both input and output data, which prevents features with larger ranges from dominating and improves convergence speed during model training. We use 3 hidden layers, each with 100 neurons and He weight initializer (He et al., 2015), along with batch normalization between layers to improve generalization. The humidity output is referred to as RHi_{ANN}. The Rectified Linear Unit (Relu) serves as the activation function for the hidden layers, while a linear function is used for the output layer. The mean squared error (MSE) is adopted as a loss function, and the ANN model is optimized using stochastic gradient descent with a learning rate of 0.001, decay of 10^{-5}, and momentum of 0.99 after several tests. Training of the ANN model is executed with batch sizes of 1024 and 100 epochs. In Sect. 2.3, four consecutive days of samples from the ERA5-IAGOS collection are allocated for model training, with the following day excluded to avoid overlap with the continuous weather system, and another day reserved either for validation, to evaluate the model's generalization to unseen data during training, or for testing. The trained model is validated against the test data set of ERA5 and IAGOS, which was previously used for comparative analysis in Sect. 2.4. To test the model's predictions, the results were transformed back to their original scale by applying the inverse of the normalization using the previously saved scaler.

Details on the preparation of training and validation data particularly for specific humidity q are provided in Sect. S3 of the supplement. Similarly, an ANN for q is implemented, with 300 neurons in each hidden layer and RHi replaced by q everywhere in the both input and output layers (refer to the supplement for more information). The ANN model can then be applied to

295 ERA5 data for humidity correction in the UTLS region. The computational time required for each scene in Fig. 1 is approx. 5 seconds on a standard laptop (Intel I5 8250U CPU; 8G memory). This technique incorporates thermodynamic and dynamical meteorological values to account for the vertical and horizontal transport of water vapor and its temporal evolution, and takes advantage of numerous humidity measurements.

3.3 Importance of the individual variables for the quality of ANN RHi prediction

300 The ANN model is interpreted with an investigation of the relative contributions of input variables to the predicted RHi_{ANN}. K_x is the relative change in loss when one input, i.e. one feature of ERA5 is set to its mean value for the complete input data set but the rest of the input features is kept unchanged:

$$K_x = \frac{L_x - L_0}{L_0} \tag{1}$$

where L_x is the loss (MSE) for the test data set compared with IAGOS when setting one ERA feature input to its average value,

305 and L_0 is the loss for the full test data set. Low values of K_x indicate a small impact of the change in input quantity on the output accuracy, or vice versa.
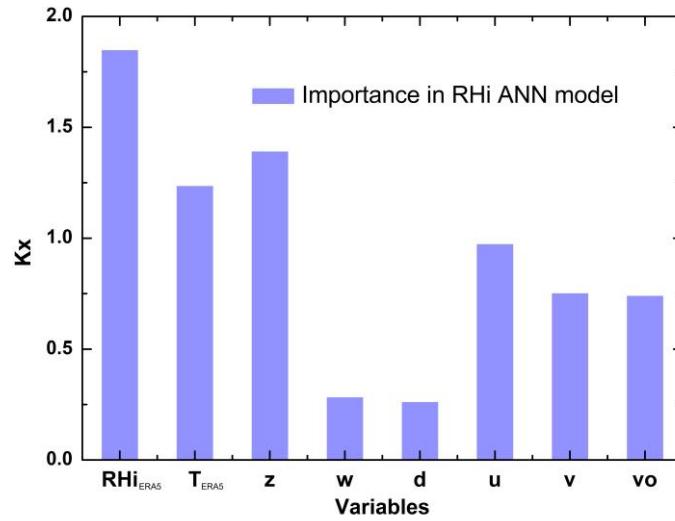
Figure 3: Relative importance of the individual variables to the ANN model for predicting RHi.

310 In Fig. 3, the importance (K_x) analysis for all input variables (the current time and level, i.e. -2 or -6 h, and -2, -1, +1, +2 levels above/below) in the ANN model reveals that RHi_{ERA5}, T_{ERA5}, and z hold the highest level of significance and carry considerable weight among all parameters. The particular relevance of these three variables can be explained by the inherent

relationship wherein RHi typically rises in regions with decreasing temperature at higher geopotential z in the troposphere. Water vapor is carried to upper altitudes with the accompanying adiabatic cooling, which increases RHi. Thus, the ANN model

315   already captures the RHi_{IAGOS} effectively using RHi_{ERA5}, T_{ERA5} and z. However, although the other (dynamical) variables are less important for the prediction of RHi_{ANN}, they provide a moderate and non-negligible contribution to the accuracy of the RHi prediction model. In fact, w and d show K_x of 0.29 and 0.26 and those for u, v, and vo even higher, which are 0.98, 0.75, and 0.74. There is generally less importance in the contributions of the variables representing dynamical quantities, aligning with the findings in Hofer et al. (2024) based on meteorological variables from the given time.

320   The fact that dynamical variables for instance particularly u, v, vo are closely as important as RHi_{ERA5}, T_{ERA5}, and z for the description of the physical processes that lead to the decrease/increase of relative humidity in Sect. S2 in the supplement but at the same time show only a moderate importance in the ANN model, could be attributed to the correlation with other variables and the significant overlap between the conditional distributions of RHi_{ERA5} on ice supersaturation determined by RHi_{IAGOS} or not (Hofer et al., 2024). Hofer et al. (2024) shows that RHi_{ERA5} is the most influential predictor for humidity predictions,

325   while the explanatory power of dynamical proxies is insufficient when only using data from the current time and level. However, our updated analysis confirms that incorporating a broader vertical region and the historical time into the dynamical variables has a more significant impact on the ANN model and contributes to the understanding of humidity evolution.

4 Model evaluation and results

4.1 Validation of ANN RHi in clear and cloudy conditions in the UTLS

330   This study aims to use the ANN model to resolve biases inherent in NWP model output evaluated in Sect. 2.4. To quantify the accuracy of the ANN model, RHi_{ANN} (and q_{ANN} in the supplement) is evaluated based on the test data set under four conditions: all sky UT, cloudy UTLS, clear sky UTLS, and all sky LS. Validation results of RHi_{ANN} are shown in Figs. 4, 5, and 6 and of q_{ANN} in Sect. S4, respectively.
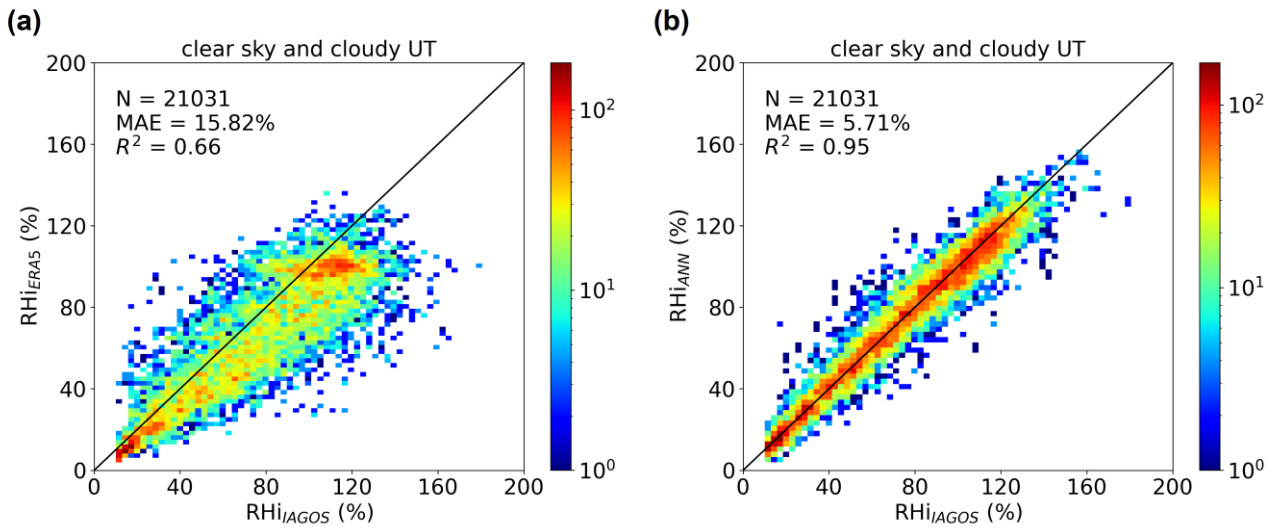
Figure 4: Distribution of (a) RHi_{ERA5} and (b) RHi_{ANN} versus RHi_{IAGOS} in the UT in all sky (clear and cloudy conditions) in the test data set. The number of data sets N, the mean absolute error MAE and the coefficient of determination R² are shown in the panels.

In the UT all sky condition important for cirrus clouds and contrails, a high number of measurements, comprising 21031 data points, are used for the inter-comparison between ERA5 and the outputs of the ANN model. RHi_{ANN} (Fig. 4b) demonstrates a better agreement with RHi_{IAGOS} compared to RHi_{ERA5} (Fig. 4a). In particular. RHi_{ANN} shows consistent values to RHi_{IAGOS} at RHi>100% which is a major improvement in comparison to the ERA5 data set. RHi_{ANN} exhibits a significant higher correlation with RHi_{IAGOS} for all uncertainty parameters (mean absolute error MAE, coefficient of determination R²) compared to ERA5. The MAE decreases significantly from 15.82% (ERA5) to 5.71% (ANN), the R^2 values increase from 0.66 (ERA5) to 0.95 (ANN), and the root mean spare error RMSE decreases from 20.52% (ERA5) to 7.88% (ANN). Notably, the ANN model also effectively corrects the existing peak at RHi_{ERA5} = 100% in Fig. 4a, and does not show a peak at RHi ~100%, similar to the IAGOS measurements. Hence the ANN exhibits a significant improvement of RHi that would be beneficial for cirrus and cloud predictions. For other scenarios, such as the cloudy UTLS, the clear sky UTLS and the all sky LS between 400 and 200 hPa, the comparison of RHi is shown in Fig. 5. Notably, also in the cloudy UTLS, RHi_{ANN} results (Fig. 5b) exhibit a closer correlation with RHi_{IAGOS} than those in the cloudy region of RHi_{ERA5} (Fig. 5a). In the cloudy (Fig. 5a-b) and clear sky (Fig. 5c-d) conditions in the UTLS, the MAE of the RHi decreases from 16.28% (11.21%) to 5.95% (4.28%), respectively. Also, the R² increases by 0.30 (0.23) to 0.95 (0.95) for the two scenarios. Again, the peak at 100% in the RHi_{ERA5} distribution in the cloudy UTLS disappears in the RHi_{ANN}, in line with the IAGOS observations. In particular, the ANN model shows a very good performance in the cloudy UTLS, and RHi_{ANN} and RHi_{IAGOS} align close to the 1:1 line. While the majority of data in the cloudy UTLS is allocated at RHi>80%, some clouds were observed in ice sub-saturated conditions, or ice particles had sedimented into dryer air.

The ANN model also has strong skills of RHi correction in the LS, see Fig. 5e and f. R^2 values increase from 0.59 (ERA5) to 0.95 (ANN), similar to the UT region in Fig. 4. The improvement of RHi prediction by the ANN is also documented by the decrease of MAE by 6.07%. The ANN model successfully learns interconnections within the data, as evident by its more accurate RHi_{ANN}.

360 Figure 6 presents a detailed relative comparison (mean bias error MBE) of either RHi_{ERA5} or RHi_{ANN} as a function of RHi_{IAGOS}. In Fig. 6a, the occurrences of $RHi_{ERA5} > 105\%$ are underestimated compared to the distribution of RHi_{IAGOS}. In Fig. 6b, the distribution of RHi_{ANN} closely resembles RHi_{IAGOS}, showing a smoother distribution around RHi of 100%. In Fig. 6c, RHi_{ERA5} shows an increasing dry bias in the UT, reaching 37% at RHi > 120%. The few data points at RHi > 120% even exhibit larger deviations by more than 60% within ERA5. As opposed to this, Fig. 6d shows that RHi_{ANN} and RHi_{IAGOS} have

365 a closer agreement, with an MBE of about ±11% for all UT measurements up to 140%. The RHi between 80% and 130% in the important range for cirrus clouds is well represented by the ANN with an MBE better than +/- 7%. This suggests that the saturated region of RHi, which presents a requisite environmental condition for new ice crystal nucleation and subsequent growth, can be more accurately parametrized.

Wolf et al. (2023) developed a humidity correction technique for RHi_{ERA5} using IAGOS measurements through a multivariate

370 quantile method. The differences between the corrected ERA5 data and RHi_{ERA5} in cloudy regions are documented in their Table 3, with the mean absolute difference ranging from -2.2% to 12.08% depending on cloud fraction. Although not directly comparable within the same timeframe, RHi_{ANN} also shows a good performance, with a MAE of approximately 5.8% in the same region of all sky UT and cloudy UTLS.

RHi_{ANN} also shows better agreement with independent airborne measurements compared to ERA5 data. For detailed

375 information on the humidity data on 21 July 2021 during the CIRRUS-HL campaign, please refer to Sect. S5 in the supplement, which includes measured data from AIMS (Atmospheric Ionization Mass Spectrometer, Kaufmann et al., 2016) instrument and RHi_{ERA5} and RHi_{ANN}.

The investigations related to validating ANN q in clear and cloudy conditions in the ULTS are shown in Sect. S4 in the supplement.
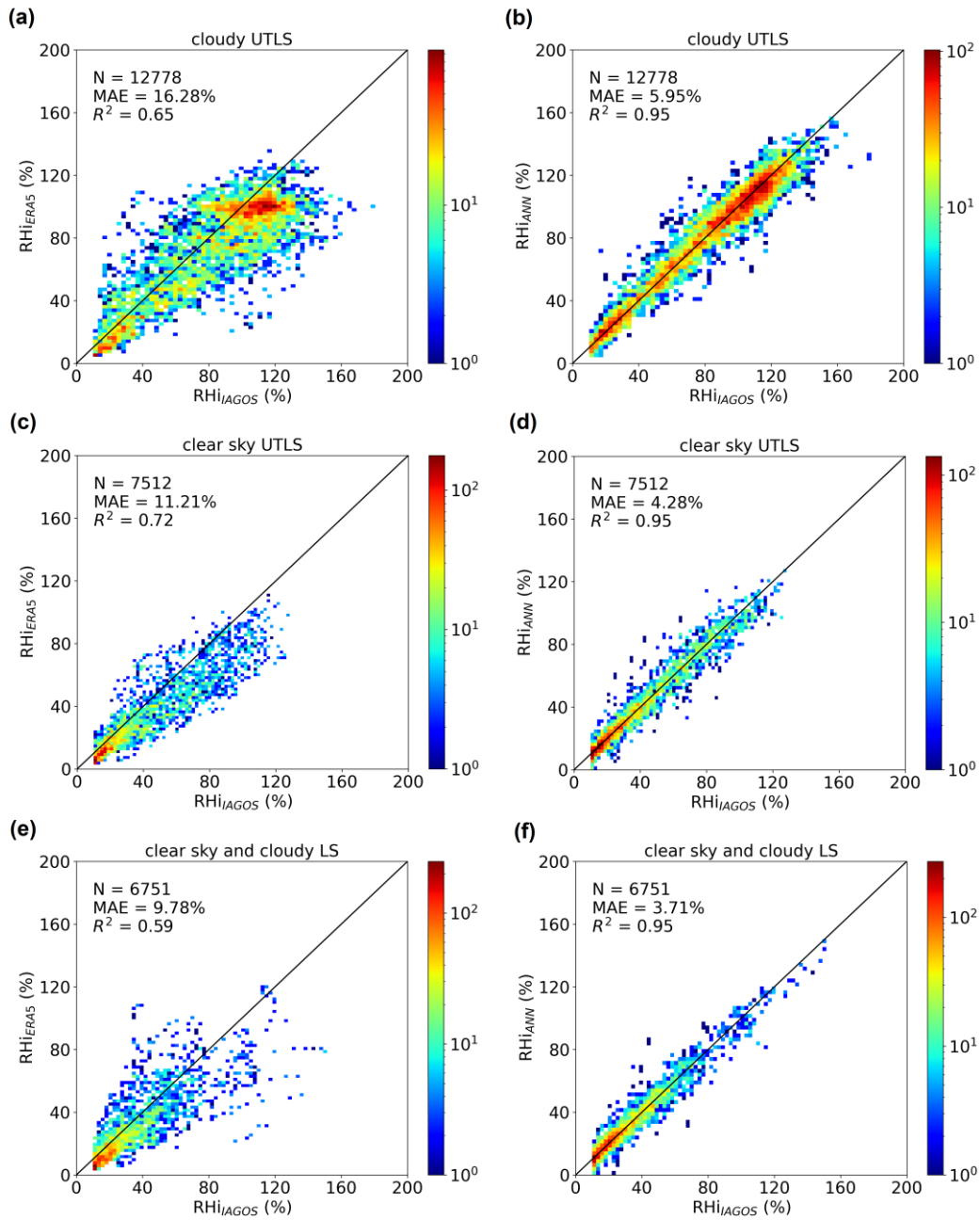
380

Figure 5: Comparison of RHi_{ERA5} (left column) and RHi_{ANN} (right column) against RHi_{IAGOS} in the (a) and (b) cloudy UTLS, (c) and (d) clear sky UTLS, and (e) and (f) clear sky and cloudy (or all sky) LS regions in the test data set. The number of data sets N, the mean absolute error MAE and the coefficient of determination R² are indicated in the individual panels.
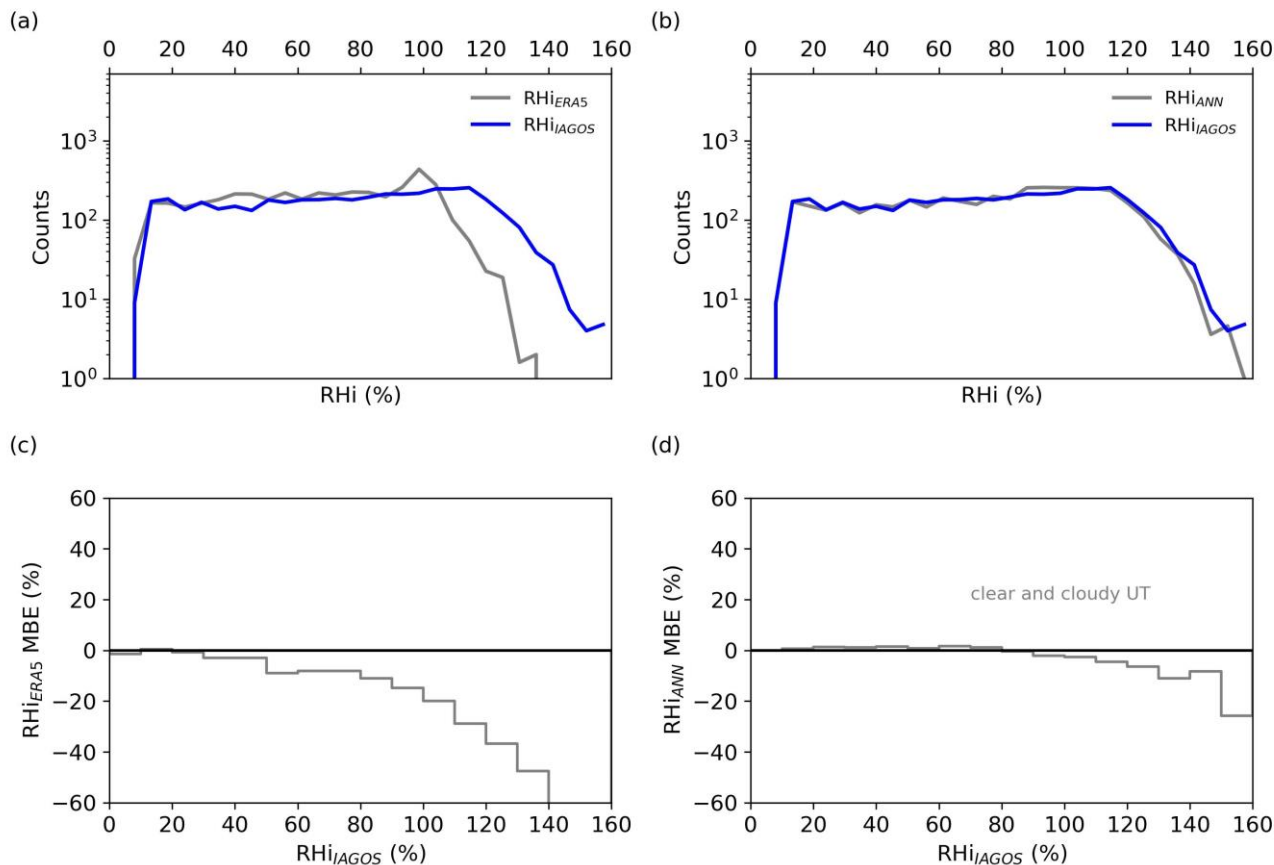
Figure 6: Frequency distribution (a and c) and overall mean biased error MBE (%) (b and d) of RHi_{ERA5} and RHi_{ANN} against RHi_{IAGOS} in the clear and cloudy UT (grey) in the test data set.

4.2 Skill of ANN and ERA5 prediction of RHi>100% versus IAGOS data

For cirrus clouds and contrails, accurately representing RHi>100%, and thus ice supersaturation, is of great importance. Hence, we focus here on the data sets with RHi>100%. The skill of ice supersaturation prediction from RHi_{ERA5} and RHi_{ANN} is evaluated based on the equitable threat score (ETS), as described in Gierens et al. (2020). The ETS measures forecasting performance by assessing the proportion of correctly forecasted events and is often used in weather forecast verification (Wang, 2014). First, events are labeled according to the contingency table, with a (Y_{IAGOS}/Y_{ERA5} or Y_{IAGOS}/Y_{ANN}, ice supersaturation predicted and observed), b (Y_{IAGOS}/N_{ERA5} or Y_{IAGOS}/N_{ANN}, no ice supersaturation predicted but observed), c (N_{IAGOS}/Y_{ERA5} or N_{IAGOS}/Y_{ANN}, ice supersaturation predicted but not observed), and d (N_{IAGOS}/N_{ERA5} or N_{IAGOS}/N_{ANN} ice supersaturation neither predicted nor observed). Y_{IAGOS} indicates that the waypoint is in ice supersaturation based on the IAGOS measurements, while N_{IAGOS} indicates the absence of ice supersaturation. The same notations are applied when analyzing the statistics for ERA5 and ANN. The ETS is then calculated using the following equations:

$$ETS = \frac{a - r}{a + b + c - r} \tag{2}$$

with

$$r = \frac{(a + b)(a + c)}{a + b + c + d} \tag{3}$$

The ETS value gets larger when the ice supersaturation prediction is closer to the measured values (here IAGOS data). ETS = 1 indicates that all RHi_{IAGOS} perfectly agree with RHi_{ERA5} or RHi_{ANN}. ETS = 0 means a completely random distribution, while negative ETS implies a negative correlation.

Table 2: ETS values for the prediction of RHi>100% from RHi_{ERA5} and RHi_{ANN} in the test data set between 200 hPa and 400 hPa over the Atlantic, Europe and Africa in 2020.

Scenarios	Y_{IAGOS}/Y_{ERA5}	Y_{IAGOS}/N_{ERA5}	N_{IAGOS}/Y_{ERA5}	N_{IAGOS}/N_{ERA5}	ETS
clear and cloudy UT	66.34%	3.31%	19.42%	10.94%	0.23
cloudy UTLS	54.61%	4.99%	24.06%	16.34%	0.21
clear and cloudy LS	97.48%	0.21%	1.96%	0.36%	0.14
clear sky UTLS	95.43%	0.05%	4.23%	0.28%	0.06

Scenarios	Y_{IAGOS}/Y_{ANN}	Y_{IAGOS}/N_{ANN}	N_{IAGOS}/Y_{ANN}	N_{IAGOS}/N_{ANN}	ETS
clear and cloudy UT	67.07%	2.57%	4.57%	25.79%	0.71
cloudy UTLS	56.26%	3.34%	4.95%	35.44%	0.70
clear and cloudy LS	97.29%	0.40%	0.89%	1.42%	0.52
clear sky UTLS	94.99%	0.49%	2.07%	2.44%	0.47

Table 2 shows ETS values for both the ERA5 and the ANN predicted ice supersaturation across all test data set in Sect. 2.4. The scores for ERA5 in all sky UT, cloudy UTLS, and all sky LS classes are 0.23, 0.21, and 0.14, respectively, indicating limited predictive skill, particularly in the all sky LS region. In contrast, the ANN model significantly enhances the ice supersaturation prediction, yielding scores of 0.71, 0.70, and 0.52 for the respective regions. This represents an approximate 0.44 increase in ETS across all classes, thereby facilitating related studies on the formation and persistence of cirrus clouds. The clear sky UTLS region is not discussed here, as we are focusing on RHi > 100%. According to Fig. 5c, few ERA5 data points fall within the ice supersaturation region in the clear sky data sets.

Teoh et al. (2022) developed a statistical approach to correct the ERA5 humidity fields in particular for ice supersaturation, with the aim of adjusting the PDF of RHi_{ERA5} in order to achieve a similar PDF as RHi_{IAGOS}. After applying this humidity correction method, the ETS for ice supersaturation in the all-sky UTLS reached a value of 0.424 when compared to IAGOS measurements in 2019, as shown in their Table S4. This statistical method outperforms RHi_{ERA5} in predicting ice supersaturation, as the latter achieves an ETS of approximately 0.2. In a recent study, Hofer et al. (2024) use RHi_{ERA5}, T_{ERA5}

and dynamical proxies only from the given time in several regression models to predict RHi>100%, and find the best regression with an ETS of 0.378 for 16588 flights of the Measurement of Ozone and Water Vapour on Airbus In-service Aircraft (MOZAIC) between 2000 and 2009. While not directly comparable within the same time frame, RHi_{ANN} excels in forecasting ice supersaturation relative to ERA5 and methods from Teoh et al. (2022) and Hofer et al. (2024), demonstrating a higher accuracy with an ETS as high as 0.71.

5 CoCiP predictions and MSG contrail cirrus observations

As an application, this section investigates the impact of improved humidity prediction in the UT on the estimation of contrail cirrus optical thickness using CoCiP simulations (Sect. 2.5) and compares the results with retrieved IOT from MSG observations using the CiPS algorithm (Sect. 2.6). The selected case is from 10 UTC on 14 April 2021 (during the ECLIF3 campaign) over the North Atlantic Region (NAR, Sect. 2.1), representing typical contrail cirrus situation just off the coast of Ireland. The MSG observation scene is from 09:45 UTC, as SEVIRI scans from the south, taking about 12 minutes per scene and reaching the upper edge (near the NAR) around 09:56 UTC, which is more consistent with the CoCiP simulation time. For the CoCiP simulations, specific humidity q_{IFS} and other atmospheric trace gas profiles from the ECMWF IFS model level data between level 73 (about 190 hPa) and level 90 (about 400 or 410 hPa) are used as input to the ANN model to produce q_{ANN} profiles. We perform two CoCiP experiments: the q_{IFS} and the resulting q_{ANN} profiles serve as input for CoCiP, respectively, while other parameters, particularly cloud liquid water content and *ciwc*, are kept constant using IFS values to include the same natural cloud effects in both CoCiP simulations.

Figure 7 provides a comparison of the spatial distributions and frequency of occurrence (histogram) of CoCiP-simulated and MSG-observed IOT. In the MSG scene (Fig. 7a), contrails and contrail cirrus, represented by linear structures with IOT ~ 0.3-0.5, are situated above the Atlantic Ocean, extending from west to east and surrounded by thicker cirrus clouds with higher IOT (even exceeding 1.0). The simulated IOTs (Figs. 7b and c) show patterns of higher IOT surrounded by lower IOT cirrus as in the MSG observations, although the single structures are not directly comparable. In addition, due to satellite detection limitations, CiPS cannot capture the thinnest ice clouds. For these reasons, a quantitative pixel-to-pixel comparison between the CoCiP simulations and the MSG observation is not meaningful in this context and we thus rather consider frequency distributions of IOT in the following. In general, the simulated IOT using q_{ANN} (Fig. 7b) is closer to CiPS retrieved IOT compared to the CoCiP simulation with q_{IFS} (Fig. 7c). The histogram (Fig. 7d) shows decreasing frequencies of occurrence with increasing IOT. The better agreement is also exhibited between IOT from CiPS and the CoCiP simulation using q_{ANN} than that using q_{IFS}. For natural cirrus, larger IOT (~0.75) is observed, while the smaller IOT (< 0.5) for contrails is of particular interest. In the lower panels showing only contrails, the simulation with increased humidity exhibits larger IOT (Fig. 7e) compared to that without humidity correction (Fig. 7f). Higher IOT up to 0.85 from CoCiP with q_{ANN}, compared to IOT values below 0.5 with q_{IFS}, is due to the growth of contrail ice crystals from the increased amount of available water vapor in q_{ANN} and is also evident in the frequency analysis (Fig. 7g).
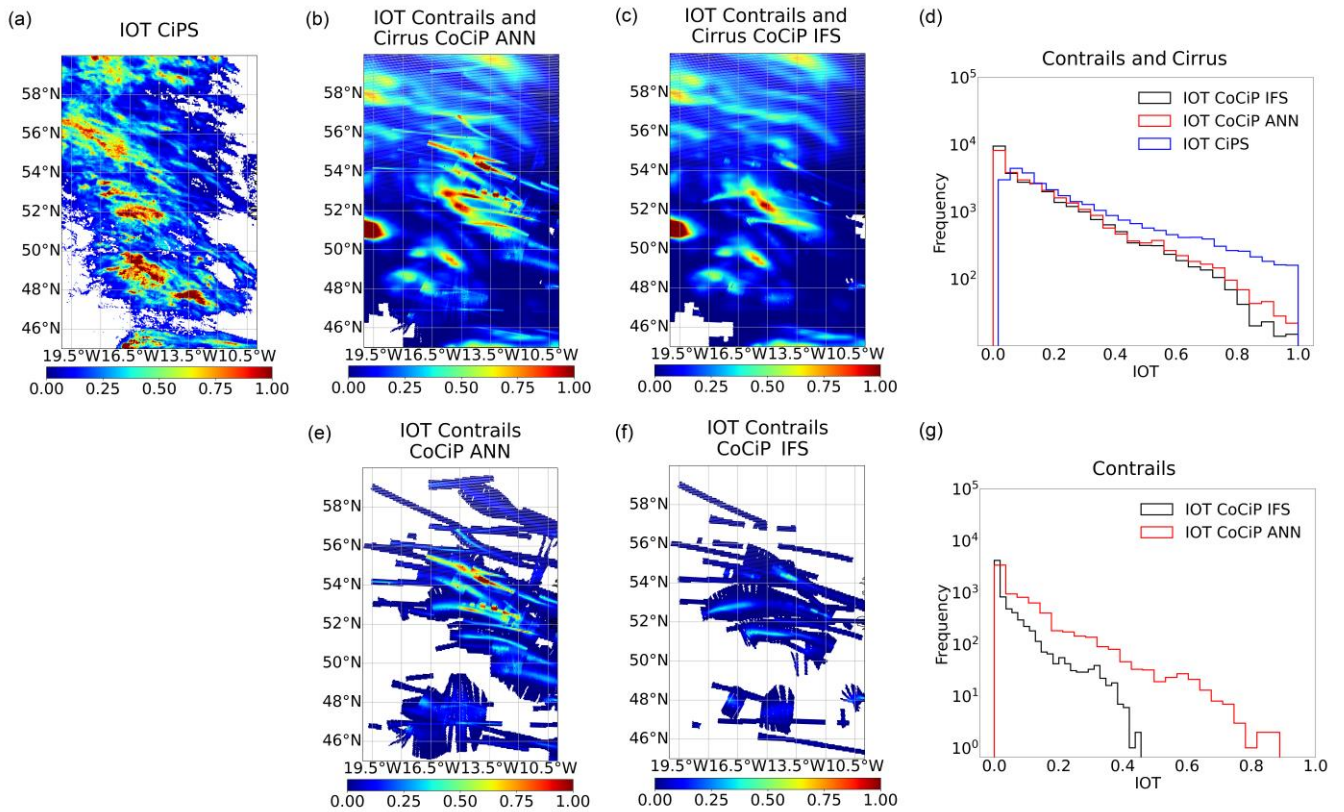
Figure 7: Distributions of IOT for contrails and cirrus retrieved from (a) MSG observations using the CiPS algorithm, and simulated using the CoCiP model with (b) q_{ANN} or (c) q_{IFS} at 10:00 UTC on 14 April 2021. The IOT distribution for contrails from CoCiP simulations is shown in (e) and (f). The IOT frequencies (histograms) for contrail cirrus and contrails are shown in (d) and (g), respectively.

In general, the model results demonstrate increased consistency with MSG observations when q_{ANN} is incorporated in CoCiP. Given that ice supersaturation typically exhibits large horizontal but shallow vertical extensions (Spichtinger et al., 2003), a minor adjustment in cruising altitude, avoiding regions of high humidity, can potentially reduce contrail radiative forcing. An improved representation of humidity thanks to an ANN approach is thus crucial for more accurate predictions of the contrail cirrus cover and radiative effect (Kaufmann et al., 2024).

6 Summary and conclusions

The distribution of relative humidity in the UTLS from NWP models, which plays a vital role in the parameterizations of natural cirrus and contrail cirrus properties, is subject to large uncertainties. In this study we propose a humidity bias correction method for relative humidity from ERA5, RHi_{ERA5}, particularly for ice supersaturation in the UT, using an ANN technique.

The novelty of this study lies in the incorporation of thermodynamic and dynamical atmospheric quantities for the given time and height together with atmospheric properties from previous times and nearby altitudes. The atmospheric humidity improvement method consists of an ANN developed using atmospheric variables from ERA5, along with collocated measurements of water vapor from IAGOS. The ERA5 data includes temporal and vertical dependencies of humidity on meteorological conditions, combining not only the historic data (-6 h, -2 h) and current time but also ±2 ERA5 pressure layers around the flight latitude of IAGOS. The target region covers the Atlantic, Europe and Africa, spanning 0 to 80°N and 30°W to 50°E and pressure levels from 400 to 200 hPa.

The analysis of biases between collocated RHi_{ERA5} and RHi_{IAGOS} reveals an underestimation of RHi_{ERA5} within the UT and an RHi occurrence peak near 100% due to the cloud saturation adjustment by ECMWF NWP. The ERA5-IAGOS collocated data is processed and the variables for training the ANN model for humidity correction are selected based on the discussion of the temporal evolution of meteorological variables. Humidity, temperature, and geopotential (as a variable for the altitude) have a main impact on the RHi_{ANN} results, while other meteorological variables, including horizontal wind speed, relative vorticity, vertical velocity, and divergence, have a high or moderate to minor but measurable influence.

Using this ANN humidity correction, the MAE of RHi_{ANN} when comparing to RHi_{ERA5} both against RHi_{IAGOS} is reduced from 15.82% to 5.71%, 16.28% to 5.95%, 11.21% to 4.28%, and 9.78% to 3.71%, in all sky UT, cloudy UTLS, clear UTLS, and all sky LS regions, respectively, presenting remarkable improvements, particularly in the all sky UT and cloudy UTLS regions. A previously existing occurrence peak at RHi = 100 % in RHi_{ERA5}, which is caused by the cloud saturation adjustment in NWP, has been removed completely by the ANN.

The representation of ice supersaturation in RHi_{ERA5} and RHi_{ANN} with respect to RHi_{IAGOS} was assessed with the calculation of the ETS value. The dynamic-based humidity correction leads to an increase in ETS from 0.23, 0.21, and 0.14 (ERA5) to 0.71, 0.70, and 0.52 by the ANN, respectively, in the all sky UT, cloudy UTLS, and all sky LS regions. The skill of ice supersaturation prediction improves considerably.

The forecast of optical and radiative properties of cirrus and contrail cirrus, based on the ANN humidity correction, is exemplarily assessed with CoCiP simulations using IFS weather data and the ANN corrected data and MSG satellite observations for one case between 35°N and 60°N (over the NAR) at 10:00 UTC on 14 April 2021. The result shows better agreement in ice optical thickness between model simulations with humidity correction and satellite observations in this contrail situation.

Teoh et al. (2022) and Wolf et al. (2023) utilize IAGOS measurements to correct RHi_{ERA5} with statistical methods. Our study shows the potential of the emerging field of machine learning-based weather prediction post-processing, in which forecast outputs are improved using historical observations and analysis data. How the current atmospheric states influence the future development of humidity patterns has been highlighted. One issue in the existing model data, where the frequency and degree of ice supersaturation in the UT are consistently underestimated due to the practice of the cloud saturation adjustment has been successfully addressed by the ANN model. The method demonstrates competitive performance, as seen by the decreased MAE and larger ETS compared to the accuracy of the aforementioned statistical methods.

Incorporating more water vapor data from the fleet-wide observations of humidity within the UTLS can further improve this method. Our findings suggest potential applications for aircraft diversion strategies to avoid ice supersaturation regions and reduce contrail cirrus climate impact. Further research on applying humidity correction methods to weather forecasts is vital for improving our understanding of the global cloud radiation budget. Our improved humidity predictions could serve as benchmarks for the measurements of further aircraft campaigns, as the assimilation or reference data set for NWP or climate models for a better parameterization of ice supersaturation. The method could also be applied to other weather forecast models, including those from ECMWF and national Weather Services. Additionally, increased resolution of NWP models at the tropopause is required for better cirrus and contrail forecasting. Combining modelled meteorological conditions and their temporal changes, along with measured humidity from long-term data sets, is essential for a more realistic representation of RHi and the subsequent processes like cloud and contrail formation in the UTLS, and their climate impact.

Data availability

IAGOS measurements are available at https://iagos.aeris-data.fr/ (IAGOS database). The ERA5 and IFS atmospheric profiles are obtained from Climate Data Store (https://cds.climate.copernicus.eu/) or ECMWF directly. The SEVIRI data are provided by EUMETSAT (European Organisation for the Exploitation of Meteorological Satellites). The CoCiP model code can be accessed from https://py.contrails.org/install.html. The machine learning technique implementation is based on the open-source platform TensorFlow (https://www.tensorflow.org). The required software packages are Python (https://www.python.org), Keras (https://pypi.org/project/keras/), and Scikit-learn (https://pypi.org/project/scikit-learn/).

Author contributions

ZW conceived the study concept, developed the methods, and wrote the paper. LB and CV advised the study and provided feedback on the paper. KG contributed to explanations of the dependence of humidity on meteorological conditions. MIH contributed to the initial method and ERA5 data evaluation. SR and AP coordinated the IAGOS research infrastructure and provided the data. SK helped with the interpretation of humidity bias in ERA5. All authors contributed to and commented on the paper.

Competing interests

One of the (co-)authors is a member of the editorial board of *Atmospheric Chemistry and Physics*. The peer-review process is guided by an independent editor, and the authors have no other competing interests to declare.

Acknowledgements

We thank the IAGOS European Research Infrastructure for excellent global aircraft measurements and ECMWF and EUMETSAT for providing the modeled atmospheric data and MSG/SEVIRI observations. ZW was supported by the DLR (Deutsches Zentrum für Luft- und Raumfahrt) / DAAD (Deutscher Akademischer Austauschdienst) Research Fellowships –

535 Doctoral Studies in Germany, 2020 under grant no 57540125 and now by the LUFO project MEFKON. CV, LB and SK are supported by the Deutsche Forschungsgemeinschaft (DFG, German Research Foundation) within SPP-1294 HALO under project no VO1504/9-1; 522359172, and TRR 301 – Project ID 428312742, and by European Union CONCERTO and by SESAR JU CICONIA. IAGOS data were created with support from the European Commission, national agencies in Germany (BMBF), France (MESR), and the UK (NERC), and the IAGOS member institutions (http://www.iagos.org/partners). The

540 participating airlines (in the year 2020: Deutsche Lufthansa, Air France, China Airlines, Hawaiian Airlines) supported IAGOS by carrying the measurement equipment free of charge. The data are available at http://www.iagos.fr thanks to additional support from AERIS. We thank Andreas Schäfler from DLR for valuable discussions.

References

545 Alduchov, O.A. and Eskridge, R.E.: Improved Magnus form approximation of saturation vapor pressure, J. Climatol. Appl. Meteorol., 35, 601–609, https://doi.org/10.1175/1520-0450(1996)035<0601:imfaos>2.0.co;2, 1996.

Berkes, F., Neis, P., Schultz, M. G., Bundke, U., Rohs, S., Smit, H. G. J., Wahner, A., Konopka, P., Boulanger, D., Nédélec, P., Thouret, V., and Petzold, A.: In situ temperature measurements in the upper troposphere and lowermost stratosphere from 2 decades of IAGOS long-term routine observation, Atmos. Chem. Phys., 17, 12495–12508, https://doi.org/10.5194/acp-17-
550 12495-2017, 2017.

Bickel, M., Ponater, M., Bock, L., Burkhardt, U., and Reineke, S.: Estimating the effective radiative forcing of contrail cirrus, J. Climate, 33, 1991–2005, https://doi.org/10.1175/JCLI-D-19-0467.1, 2020.

Burkhardt, U., Bock, L., and Bier, A.: Mitigating the contrail cirrus climate impact by reducing aircraft soot number emissions, npj Clim. Atmos. Sci., 1, 37, https://doi.org/10.1038/s41612-018-0046-4, 2018.

555 Chen, C.-C., Gettelman, A., Craig, C., Minnis, P., and Duda, D. P.: Global contrail coverage simulated by CAM5 with the inventory of 2006 global aircraft emissions, J. Adv. Model. Earth Syst., 4, M04003, https://doi.org/10.1029/2011MS000105, 2012.

Dessler, A. E. and Sherwood, S. C.: ATMOSPHERIC SCIENCE: A Matter of Humidity, Science, 323, 1020–1021, https://doi.org/10.1126/science.1171264, 2009.

560 Diao, M., Jensen, J. B., Pan, L. L., Homeyer, C. R., Honomichl, S., Bresch, J. F., and Bansemer, A.: Distributions of ice supersaturation and ice crystals from airborne observations in relation to upper tropospheric dynamical boundaries, J. Geophys. Res.-Atmos., 120, 5101–5121, https://doi.org/10.1002/2015JD023139, 2015.

Dickson, N. C., Gierens, K. M., Rogers, H. L., and Jones, R. L.: Probabilistic description of ice-supersaturated layers in low resolution profiles of relative humidity, Atmos. Chem. Phys., 10, 6749–6763, https://doi.org/10.5194/acp-10-6749-2010, 2010.

565 Dyroff, C., Zahn, A., Christner, E., Forbes, R., Tompkins, A. M., and van Velthoven, P. F. J.: Comparison of ECMWF analysis and forecast humidity data with CARIBIC upper troposphere and lower stratosphere observations, Q. J. Roy. Meteor. Soc., 141, 833–844, https://doi.org/10.1002/qj.2400, 2015.

ECMWF.: IFS Documentation CY41R2 - Part IV: Physical Processes, IFS Documentation CY41R2, 4, https://doi.org/10.21957/tr5rv27xu, 2016.

570   Forbes, R. M. and Ahlgrimm, M.: On the representation of high-latitude boundary layer mixed-phase cloud in the ECMWF global model, Mon. Weather Rev., 142, 3425–3445, https://doi.org/10.1175/MWR-D-13-00325.1, 2014.

Forbes, R. and Tompkins, A.: An improved representation of cloud and precipitation, Tech. Rep., European Center for Medium-Range Weather Forecasting, https://doi.org/10.21957/nfgulzhe, 2011.

Forster, P. M. de F. and Shine, K. P.: Assessing the climate impact of trends in stratospheric water vapor, Geophys. Res. Lett., 575   29, 10-1–10-4, https://doi.org/10.1029/2001GL013909, 2002.

Fu, Q. and Liou, K.: On the correlated k-distribution method for radiative transfer in nonhomogeneous atmospheres, J. Atmos. Sci., 49, 2139–2156, https://doi.org/10.1175/1520-0469(1992)049<2139:OTCDMF>2.0.CO;2, 1992.

Gasparini, B., McGraw, Z., Storelvmo, T., and Lohmann, U.: To what extent can cirrus cloud seeding counteract global warming?, Environ. Res. Lett., 15, 054002, https://doi.org/10.1088/1748-9326/ab71a3, 2020.

580   Gettelman, A., Hoor, P., Pan, L. L., Randel, W. J., Hegglin, M. I., and Birner, T.: THE EXTRATROPICAL UPPER TROPOSPHERE AND LOWER STRATOSPHERE, Rev. Geophys., 49, 3, https://doi.org/10.1029/2011RG000355, 2011.

Gierens, K. and Brinkop, S.: Dynamical characteristics of ice supersaturated regions, Atmos. Chem. Phys., 12, 11933–11942, https://doi.org/10.5194/acp-12-11933-2012, 2012.

Gierens, K., Matthes, S., and Rohs, S.: How Well Can Persistent Contrails Be Predicted?, Aerospace, 7, 169, 585   https://doi.org/10.3390/aerospace7120169, 2020.

Groß, S., Wirth, M., Schäfler, A., Fix, A., Kaufmann, S., and Voigt, C.: Potential of airborne lidar measurements for cirrus cloud studies, Atmos. Meas. Tech., 7, 2745–2755, https://doi.org/10.5194/amt-7-2745-2014, 2014.

He, K., Zhang, X., Ren, S., and Sun, J.: Delving Deep into Rectifiers: Surpassing Human-Level Performance on ImageNet Classification, 2015 IEEE International Conference on Computer Vision (ICCV), Santiago, Chile, 1026-1034, 590   https://doi.org/10.1109/ICCV.2015.123, 2015.

Hegglin, M. I., Plummer, D. A., Shepherd, T. G., Scinocca, J. F., Anderson, J., Froidevaux, L., Funke, B., Hurst, D., Rozanov, A., Urban, J., von Clarmann, T., Walker, K. A., Wang, H. J., Tegtmeier, S., and Weigel, K.: Vertical structure of stratospheric water vapour trends derived from merged satellite data, Nat. Geosci., 7, 768–776, https://doi.org/10.1038/NGEO2236, 2014.

Hegglin, M. I., Tegtmeier, S., Anderson, J., Froidevaux, L., Fuller, R., Funke, B., Jones, A., Lingenfelser, G., Lumpe, J., 595   Pendlebury, D., Remsberg, E., Rozanov, A., Toohey, M., Urban, J., von Clarmann, T., Walker, K. A., Wang, R., and Weigel, K.: SPARC data initiative: Comparison of water vapor climatologies from international satellite limb sounders: Sparc Data Initiative Water Vapor Comparisons, J. Geophys. Res.-Atmos., 118, 11824–11846, https://doi.org/10.1002/jgrd.50752, 2013.

Hersbach, H., Bell, B., Berrisford, P., Hirahara, S., Horányi, A., Muñoz-Sabater, J., Nicolas, J., Peubey, C., Radu, R., Schepers, D., Simmons, A., Soci, C., Abdalla, S., Abellan, X., Balsamo, G., Bechtold, P., Biavati, G., Bidlot, J., Bonavita, M., De Chiara, 600   G., Dahlgren, P., Dee, D., Diamantakis, M., Dragani, R., Flemming, J., Forbes, R., Fuentes, M., Geer, A., Haimberger, L., Healy, S., Hogan, R. J., Hólm, E., Janisková, M., Keeley, S., Laloyaux, P., Lopez, P., Lupu, C., Radnoti, G., de Rosnay, P.,

Rozum, I., Vamborg, F., Villaume, S., and Thépaut, J.-N.: The ERA5 Global Reanalysis, Q. J. Roy. Meteor. Soc., 146, 1999–2049, https://doi.org/10.1002/qj.3803, 2020.

Heymsfield, A. J., Miloshevich, L. M., Twohy, C., Sachse, G., and Oltmans, S.: Upper-tropospheric relative humidity observations and implications for cirrus ice nucleation, Geophys. Res. Lett., 25, 1343–1346, https://doi.org/10.1029/98GL01089, 1998.

Hofer, S., Gierens, K., and Rohs, S.: How well can persistent contrails be predicted? An update, Atmos. Chem. Phys., 24, 7911–7925, https://doi.org/10.5194/acp-24-7911-2024, 2024.

Kärcher, B.: Formation and radiative forcing of contrail cirrus, Nat. Commun., 9, 1824, https://doi.org/10.1038/s41467-018-04068-0, 2018.

Kaufmann, S., Dischl, R., and Voigt, C.: Regional and seasonal impact of hydrogen propulsion systems on potential contrail cirrus cover, Atmos. Environ.: X, 24, 100298, https://doi.org/10.1016/j.aeaoa.2024.100298, 2024.

Kaufmann, S., Voigt, C., Jurkat, T., Thornberry, T., Fahey, D. W., Gao, R.-S., Schlage, R., Schäuble, D., and Zöger, M.: The airborne mass spectrometer AIMS – Part 1: AIMS-H2O for UTLS water vapor measurements, Atmos. Meas. Tech., 9, 939–953, https://doi.org/10.5194/amt-9-939-2016, 2016.

Kaufmann, S., Voigt, C., Heller, R., Jurkat-Witschas, T., Krämer, M., Rolf, C., Zöger, M., Giez, A., Buchholz, B., Ebert, V., Thornberry, T., and Schumann, U.: Intercomparison of midlatitude tropospheric and lower-stratospheric water vapor measurements and comparison to ECMWF humidity data, Atmos. Chem. Phys., 18, 16729–16745, https://doi.org/10.5194/acp-18-16729-2018, 2018.

Krämer, M., Schiller, C., Afchine, A., Bauer, R., Gensch, I., Mangold, A., Schlicht, S., Spelten, N., Sitnikov, N., Borrmann, S., de Reus, M., and Spichtinger, P.: Ice supersaturations and cirrus cloud crystal numbers, Atmos. Chem. Phys., 9, 3505–3522, https://doi.org/10.5194/acp-9-3505-2009, 2009.

Krüger, K., Schäfler, A., Wirth, M., Weissmann, M., and Craig, G. C.: Vertical structure of the lower-stratospheric moist bias in the ERA5 reanalysis and its connection to mixing processes, Atmos. Chem. Phys., 22, 15559–15577, https://doi.org/10.5194/acp-22-15559-2022, 2022.

Kadow, C., Hall, D. M., and Ulbrich, U.: Artificial intelligence reconstructs missing climate information, Nat. Geosci., 13, 408–413, https://doi.org/10.1038/s41561-020-0582-5, 2020.

Kunz, A., Spelten, N., Konopka, P., Müller, R., Forbes, R. M., and Wernli, H.: Comparison of Fast In situ Stratospheric Hygrometer (FISH) measurements of water vapor in the upper troposphere and lower stratosphere (UTLS) with ECMWF (re)analysis data, Atmos. Chem. Phys., 14, 10803–10822, https://doi.org/10.5194/acp-14-10803-2014, 2014.

Lam, R., Sanchez-Gonzalez, A., Willson, M., Wirnsberger, P., Fortunato, M., Alet, F., Ravuri, S., Ewalds, T., Eaton-Rosen, Z., Hu, W., Merose, A., Hoyer, S., Holland, G., Vinyals, O., Stott, J., Pritzel, A., Mohamed, S., and Battaglia, P.: Learning skillful medium-range global weather forecasting, Science, 382, 1416-1421, https://doi.org/10.1126/science.adi2336, 2023.

Lamquin, N., Stubenrauch, C. J., Gierens, K., Burkhardt, U., and Smit, H.: A global climatology of upper-tropospheric ice supersaturation occurrence inferred from the Atmospheric Infrared Sounder calibrated by MOZAIC, Atmos. Chem. Phys., 12, 381–405, https://doi.org/10.5194/acp-12-381-2012, 2012.

Lawrence, H., Bormann, N., Sandu, I., Day, J., Farnan, J., and Bauer, P.: Use and impact of Arctic observations in the ECMWF Numerical Weather Prediction system, Q. J. Roy. Meteor. Soc., 145, 3432–3454, https://doi.org/10.1002/qj.3628, 2019.

Ma, R., Letu, H., Yang, K., Wang, T., Shi, C., Xu, J., Shi, J., Shi, C., and Chen, L.: Estimation of surface shortwave radiation from Himawari-8 satellite data based on a combination of radiative transfer and deep neural network, IEEE T. Geosci. Remote, 58, 5304–5316, https://doi.org/10.1109/tgrs.2019.2963262, 2020.

Märkl, R. S., Voigt, C., Sauer, D., Dischl, R. K., Kaufmann, S., Harlaß, T., Hahn, V., Roiger, A., Weiß-Rehm, C., Burkhardt, U., Schumann, U., Marsing, A., Scheibe, M., Dörnbrack, A., Renard, C., Gauthier, M., Swann, P., Madden, P., Luff, D., Sallinen, R., Schripp, T., and Le Clercq, P.: Powering aircraft with 100 % sustainable aviation fuel reduces ice crystals in contrails, Atmos. Chem. Phys., 24, 3813–3837, https://doi.org/10.5194/acp-24-3813-2024, 2024.

Sanogo, S., Boucher, O., Bellouin, N., Borella, A., Wolf, K., and Rohs, S.: Variability in the properties of the distribution of the relative humidity with respect to ice: implications for contrail formation, Atmos. Chem. Phys., 24, 5495–5511, https://doi.org/10.5194/acp-24-5495-2024, 2024.

Mannstein, H., Brömser, A., and Bugliaro, L.: Ground-based observations for the validation of contrails and cirrus detection in satellite imagery, Atmos. Meas. Tech., 3, 655–669, https://doi.org/10.5194/amt-3-655-2010, 2010.

Petzold, A., Thouret, V., Gerbig, C., Zahn, A., Brenninkmeijer, C. A. M., Gallagher, M., Hermann, M., Pontaud, M., Ziereis, H., Boulanger, D., Marshall, J., Nédélec, P., Smit, H. G. J., Frieß, U., Flaud, J.-M., Wahner, A., Cammas, J.-P., Volz-Thomas, A., and IAGOS-Team: Global-Scale Atmosphere Monitoring by In-Service Aircraft – Current Achievements and Future Prospects of the European Research Infrastructure IAGOS, Tellus B, 67, 28452, https://doi.org/10.3402/tellusb.v67.28452, 2015.

Petzold, A., Neis, P., Rütimann, M., Rohs, S., Berkes, F., Smit, H. G. J., Krämer, M., Spelten, N., Spichtinger, P., Nédélec, P., and Wahner, A.: Ice-supersaturated air masses in the northern mid-latitudes from regular in situ observations by passenger aircraft: vertical distribution, seasonality and tropospheric fingerprint, Atmos. Chem. Phys., 20, 8157–8179, https://doi.org/10.5194/acp-20-8157-2020, 2020.

Reutter, P., Neis, P., Rohs, S., and Sauvage, B.: Ice supersaturated regions: properties and validation of ERA-Interim reanalysis with IAGOS in situ water vapour measurements, Atmos. Chem. Phys., 20, 787–804, https://doi.org/10.5194/acp-20-787-2020, 2020.

Riese, M., Ploeger, F., Rap, A., Vogel, B., Konopka, P., Dameris, M., and Forster, P.: Impact of uncertainties in atmospheric mixing on simulated UTLS composition and related radiative effects, J. Geophys. Res., 117, D16305, https://doi.org/10.1029/2012JD017751, 2012.

Rollins, A. W., Thornberry, T. D., Gao, R. S., Smith, J. B., Sayres, D. S., Sargent, M. R., Schiller, C., Krämer, M., Spelten, N., Hurst, D. F., Jordan, A. F., Hall, E. G., Vömel, H., Diskin, G. S., Podolske, J. R., Christensen, L. E., Rosenlof, K. H.,

Jensen, E. J., and Fahey, D. W.: Evaluation of UT/LS hygrometer accuracy by intercomparison during the NASA MACPEX mission, J. Geophys. Res.-Atmos., 119, 1915–1935, https://doi.org/10.1002/2013JD020817, 2014.

670 Rolf, C., Rohs, S., Smit, H G.J., Krämer, M., Bozóki, Z., Hofmann, S., Franke, H., Maser, R., Hoor, P., Petzold, A.: Evaluation of compact hygrometers for continuous airborne measurements, Meteorol. Z., early access, https://doi.org/10.1127/metz/2023/1187, 2023.

Schmidt, G. A., Ruedy, R. A., Miller, R. L., and Lacis, A. A.: Attribution of the present-day total greenhouse effect, J. Geophys. Res.-Atmos., 115, D20106, https://doi.org/10.1029/2010JD014287, 2010.

675 Schumann, U.: On conditions for contrail formation from aircraft exhausts, Meteorol. Z., 5, 4–23, https://doi.org/10.1127/metz/5/1996/4, 1996.

Schumann, U.: A contrail cirrus prediction model, Geosci. Model Dev., 5, 543–580, https://doi.org/10.5194/gmd-5-543-2012, 2012.

Schumann, U., Baumann, R., Baumgardner, D., Bedka, S. T., Duda, D. P., Freudenthaler, V., Gayet, J. F., Heymsfield, A. J., 680 Minnis, P., Quante, M., Raschke, E., Schlager, H., Vázquez-Navarro, M., Voigt, C., and Wang, Z.: Properties of individual contrails: a compilation of observations and some comparisons, Atmos. Chem. Phys., 17, 403–438, https://doi.org/10.5194/acp-17-403-2017, 2017.

Schumann, U., Bugliaro, L., Dörnbrack, A., Baumann, R., and Voigt, C.: Aviation Contrail Cirrus and Radiative Forcing Over Europe During 6 Months of COVID-19, Geophys. Res. Lett., 48, e2021GL092771, https://doi.org/10.1029/2021GL092771, 685 2021a.

Schumann, U., Poll, I., Teoh, R., Koelle, R., Spinielli, E., Molloy, J., Koudis, G. S., Baumann, R., Bugliaro, L., Stettler, M., and Voigt, C.: Air traffic and contrail changes over Europe during COVID-19: a model study, Atmos. Chem. Phys., 21, 7429–7450, https://doi.org/10.5194/acp-21-7429-2021, 2021b.

Seifert, A., and Siewert, C.: An ML-based P3-like multimodal two-moment ice microphysics in the ICON model, ESS Open 690 Archive, doi: 10.22541/essoar.170689097.75412140/v1, February 02, 2024.

Sonntag, D.: Advancements in the field of hygrometry, Meteorol. Z., 3, 51–66, https://doi.org/10.1127/metz/3/1994/51, 1994.

Sperber, D. and Gierens, K.: Towards a more reliable forecast of ice supersaturation: concept of a one-moment ice-cloud scheme that avoids saturation adjustment, Atmos. Chem. Phys., 23, 15609–15627, https://doi.org/10.5194/acp-23-15609-2023, 2023.

695 Spichtinger, P., Gierens, K., and Read, W.: The global distribution of ice-supersaturated regions as seen by the Microwave Limb Sounder, Quart. J. Roy. Met. Soc., 129, 3391–3410, https://doi.org/10.1256/qj.02.141, 2003.

Stenke, A., Grewe, V., and Ponater, M.: Lagrangian transport of water vapor and cloud water in the ECHAM4 GCM and its impact on the cold bias, Clim. Dynam., 31, 491–506, https://doi.org/10.1007/s00382-007-0347-5, 2008.

Strandgren, J., Bugliaro, L., Sehnke, F., and Schröder, L.: Cirrus cloud retrieval with MSG/SEVIRI using artificial neural 700 networks, Atmos. Meas. Tech., 10, 3547–3573, https://doi.org/10.5194/amt-10-3547-2017, 2017.

Tao, M., Konopka, P., Wright, J. S., Liu, Y., Bian, J., Davis, S., Jia, Y., and Ploeger, F.: Multi-decadal variability controls short-term stratospheric water vapor trends, Commun. Earth Environ., 4, 2662–4435, https://doi.org/10.1038/s43247-023-01094-9, 2023.

705 Teoh, R., Schumann, U., Majumdar, A., and Stettler, M. E. J.: Mitigating the Climate Forcing of Aircraft Contrails by Small-Scale Diversions and Technology Adoption, Environ. Sci. Technol., 54, 2941–2950, https://doi.org/10.1021/acs.est.9b05608, 2020.

Teoh, R., Schumann, U., Gryspeerdt, E., Shapiro, M., Molloy, J., Koudis, G., Voigt, C., and Stettler, M. E. J.: Aviation contrail climate effects in the North Atlantic from 2016 to 2021, Atmos. Chem. Phys., 22, 10919–10935, https://doi.org/10.5194/acp-22-10919-2022, 2022.

710 Teoh, R., Engberg, Z., Schumann, U., Voigt, C., Shapiro, M., Rohs, S., and Stettler, M. E. J.: Global aviation contrail climate effects from 2019 to 2021, Atmos. Chem. Phys., 24, 6071–6093, https://doi.org/10.5194/acp-24-6071-2024, 2024.

Tiedtke, M.: Representation of clouds in large-scale models, Mon. Weather Rev., 121, 3040–3061, https://doi.org/10.1175/1520-0493(1993)121<3040:ROCILS>2.0.CO;2, 1993.

Tompkins, A., Gierens, K., and Rädel, G.: Ice supersaturation in the ECMWF Integrated Forecast System, Q. J. Roy. Metor. Soc., 133, 53–63, https://doi.org/10.1002/qj.14, 2007.

715 van der Linden, R., Knippertz, P., Fink, A. H., Ingleby, B., Maranan, M., and Benedetti, A.: The influence of DACCIWA radiosonde data on the quality of ECMWF analyses and forecasts over southern West Africa, Q. J. Roy. Meteor. Soc., 146, 1719–1739, https://doi.org/10.1002/qj.3763, 2020.

Voigt, C., Schumann, U., Minikin, A., Abdelmonem, A., Afchine, A., Borrmann, S., Boettcher, M., Buchholz, B., Bugliaro, 720 L., Costa, A., Curtius, J., Dollner, M., Dörnbrack, A., Dreiling, V., Ebert, V., Ehrlich, A., Fix, A., Forster, L., Frank, F., Fütterer, D., Giez, A., Graf, K., Grooß, J.-U., Groß, S., Heimerl, K., Heinold, B., Hüneke, T., Järvinen, E., Jurkat, T., Kaufmann, S., Kenntner, M., Klingebiel, M., Klimach, T., Kohl, R., Krämer, M., Krisna, T. C., Luebke, A., Mayer, B., Mertes, S., Molleker, S., Petzold, A., Pfeilsticker, K., Port, M., Rapp, M., Reutter, P., Rolf, C., Rose, D., Sauer, D., Schäfler, A., Schlage, R., Schnaiter, M., Schneider, J., Spelten, N., Spichtinger, P., Stock, P., Walser, A., Weigel, R., Weinzierl, B., 725 Wendisch, M., Werner, F., Wernli, H., Wirth, M., Zahn, A., Ziereis, H., and Zöger, M.: ML-CIRRUS: The Airborne Experiment on Natural Cirrus and Contrail Cirrus with the High-Altitude Long-Range Research Aircraft HALO, B. Am. Meteorol. Soc., 98, 271–288, https://doi.org/10.1175/BAMS-D-15-00213.1, 2017.

Voigt, C., Lelieveld, J., Schlager, H., Schneider, J., Curtius, J., Meerkötter, R., Sauer, D., Bugliaro, L., Bohn, B., Crowley, J. N., Erbertseder, T., Groß, S., Hahn, V., Li, Q., Mertens, M., Pöhlker, M. L., Pozzer, A., Schumann, U., Tomsche, L., Williams, 730 J., Zahn, A., Andreae, M., Borrmann, S., Bräuer, T., Dörich, R., Dörnbrack, A., Edtbauer, A., Ernle, L., Fischer, H., Giez, A., Granzin, M., Grewe, V., Harder, H., Heinritzi, M., Holanda, B. A., Jöckel, P., Kaiser, K., Krüger, O. O., Lucke, J., Marsing, A., Martin, A., Matthes, S., Pöhlker, C., Pöschl, U., Reifenberg, S., Ringsdorf, A., Scheibe, M., Tadic, I., Zauner-Wieczorek, M., Henke, R., and Rapp, M.: Cleaner skies during the COVID-19 lockdown, B. Am. Meteorol. Soc., 103, E1796–E1827, https://doi.org/10.1175/BAMS-D-21-0012.1, 2022.

Wang, C.-C.: On the Calculation and Correction of Equitable Threat Score for Model Quantitative Precipitation Forecasts for Small Verification Areas: The Example of Taiwan, Weather Forecast., 29, 788–798, https://doi.org/10.1175/WAF-D-13-00087.1, 2014.

Wang, Z., Bugliaro, L., Jurkat-Witschas, T., Heller, R., Burkhardt, U., Ziereis, H., Dekoutsidis, G., Wirth, M., Groß, S., Kirschler, S., Kaufmann, S., and Voigt, C.: Observations of microphysical properties and radiative effects of a contrail cirrus outbreak over the North Atlantic, Atmos. Chem. Phys., 23, 1941–1961, https://doi.org/10.5194/acp-23-1941-2023, 2023.

Wang, Z., Letu, H., Shang, H., and Bugliaro, L.: Technical note: Retrieval of the supercooled liquid fraction in mixed-phase clouds from Himawari-8 observations, Atmos. Chem. Phys., 24, 7559–7574, https://doi.org/10.5194/acp-24-7559-2024, 2024.

Wang, H. and Su, W.: Evaluating and Understanding Top of the Atmosphere Cloud Radiative Effects in Intergovernmental Panel on Climate Change (IPCC) Fifth Assessment Report (AR5) Coupled Model Intercomparison Project Phase 5 (CMIP5) Models Using Satellite Observations, J. Geophys. Res.-Atmos., 118, 683–699, https://doi.org/10.1029/2012JD018619, 2013.

Wilhelm, L., Gierens, K., and Rohs, S.: Meteorological Conditions That Promote Persistent Contrails, Appl. Sci.-Basel, 12, 4450, https://doi.org/10.3390/app12094450, 2022.

Woiwode, W., Dörnbrack, A., Polichtchouk, I., Johansson, S., Harvey, B., Höpfner, M., Ungermann, J., and Friedl-Vallon, F.: Technical note: Lowermost-stratosphere moist bias in ECMWF IFS model diagnosed from airborne GLORIA observations during winter–spring 2016, Atmos. Chem. Phys., 20, 15379–15387, https://doi.org/10.5194/acp-20-15379-2020, 2020.

Wolf, K., Bellouin, N., Boucher, O., Rohs, S., and Li, Y.: Correction of temperature and relative humidity biases in ERA5 by bivariate quantile mapping: Implications for contrail classification, EGUsphere [preprint], https://doi.org/10.5194/egusphere-2023-2356, 2023.

Zängl, G., Reinert, D., Rípodas, P., and Baldauf, M.: The ICON (ICOsahedral Non-hydrostatic) modelling framework of DWD and MPI-M: Description of the non-hydrostatic dynamical core, Q. J. Roy. Meteor. Soc., 141, 563–579, https://doi.org/10.1002/qj.2378, 2015.

Zhao, Y., Li, J., Zhang, L., Deng, C., Li, Y., Jian, B., and Huang, J.: Diurnal cycles of cloud cover and its vertical distribution over the Tibetan Plateau revealed by satellite observations, reanalysis datasets, and CMIP6 outputs, Atmos. Chem. Phys., 23, 743–769, https://doi.org/10.5194/acp-23-743-2023, 2023.